ACS APPLIED MATERIALS & INTERFACES

Research Article

www.acsami.org

Synthesis of a Novel Core–Shell Nanocomposite $Ag@SiO_2@Lu_2O_3$:Gd/Yb/Er for Large Enhancing Upconversion Luminescence and Bioimaging

Dongguang Yin,*[,†] Chengcheng Wang,[†] Juan Ouyang,[†] Xinyu Zhang,[†] Zheng Jiao,[†] Yi Feng,[‡] Kailin Song,[†] Bing Liu,[†] Xianzhang Cao,[†] Lu Zhang,[†] Yanlin Han,[†] and Minghong Wu*[,†]

[†]School of Environmental and Chemical Engineering, Shanghai University, Shanghai 200444, China

[‡]Mental Health Center of Shanghai Zhabei District, Shanghai 200436, China

Supporting Information

ABSTRACT: Upconversion nanocrystals have many advantages over other fluorescent materials. However, their upconversion luminescence intensities are not desirable, limiting their applications for highly sensitive detection. Therefore, it is really important to enhance upconversion luminescent intensities of upconversion nanocrystals. In the present study, a novel Ag core and upconversion nanocrystal shell based nanocomposite $Ag@SiO_2@Lu_2O_3$:Gd/Yb/Er for metal-enhanced upconversion luminescence was fabricated successfully, and its morphology, crystalline phase, composition, optical property, and cell imaging application were investigated. It was found that a maximum upconversion luminescence enhancement of 30-fold was obtained in comparison with the control without a silver core, and the nanocomposite exhibited bright upconversion luminescence when it was used for imaging with HeLa cells. This enhancement potentially increases the overall upconversion nanocrystal detectability, endowing the nanocomposite with a potential capability for highly sensitive biological, medical, and optical detection.

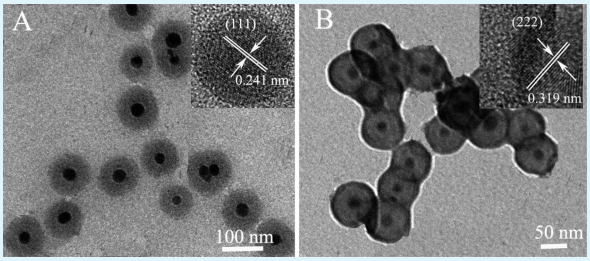

KEYWORDS: *nanocomposite $Ag@SiO_2@Lu_2O_3$:Gd/Yb/Er, enhancement upconversion luminescence, synthesis, core–shell structure, cell imaging*

1. INTRODUCTION

Upconversion nanocrystals (UCNs) have attracted much attention in recent years due to their unique optical and chemical properties. Compared to other fluorescent materials such as organic dyes and quantum dots (QDs), UCNs possess many advantages, including large anti-Stokes shifts, high signal-to-noise ratios, deep penetration, no toxicity, and high physical-chemical stability.[1−4] On the basis of their superior properties, UCNs have many potential applications, including biological imaging, display technologies, near-IR quantum counters, and so on.[5−10] However, UCNs generally suffer from low upconversion luminescence (UCL) efficiency due to structural defects, dipole forbidden transitions, and limited excitation efficiency caused by small absorption cross sections.[11,12] Thus, UCNs that can be used for highly sensitive biological and medical detections such as monomolecular determination and in vivo imaging are still limited.[13−15]

In order to enhance the upconversion emission intensity and expand their applications, some approaches, such as coating silica, fabricating core–shell structures, doping Gd^{3+} ions, and introducing noble metal nanoparticles, have been developed.[16−18] It is well-known that introducing noble metal nanoparticles for metal-enhanced fluorescence (MEF) is an efficient strategy to enhance fluorescence intensities of luminescent probes.[19−28] MEF arises from the interaction between fluorophore and plasmon resonance of metal nanoparticles (silver or gold). This results in enhancement of excitation rates through local field amplification and increasing emission efficiency by enhanced radiative decay rates, both of which contribute to an overall increase in fluorescent emission intensities.[24−26] MEF has been used as a powerful technology to increase the luminescence intensity and detection sensitivity.[27−31] MEF applied in organic dyes, quantum dots, and lanthanide complexes has been extensively studied previously.[31] The fluorescence enhancement varies from fractional (quenching) to large amplification of above 100-fold.[23] Recently, some studies applying MEF to UCNs have been reported.[28−30] It has recently been found that integrating rare earth ions-doped UCNs with noble metals such as Au or Ag nanoparticles is an active and versatile strategy to amplify fluorescence signals of UCNs.[24−26] Various UCNs-metal geometric configurations that can achieve UCL enhancement have been made recently. For example, UCL enhancements of 2.5-, 3.4-, 4-, 14.4-, 45-, and 76-fold have been obtained for $NaYF_4$:Yb,Tm@Au, $Ag@SiO_2@NaYF_4$:Gd/Yb/Er, $Ag@SiO_2@Y_2O_3$:Er, $NaYF_4$:Yb,Er@SiO_2@Ag, $Ag@Al_2O_3@NaYF_4$:Yb/Er,

Received: November 27, 2013
Accepted: October 3, 2014
Published: October 3, 2014

and Au@$NaYF_4$:Gd/Yb/Tm metal nanostructures, respectively.[6,19,26,27,32,33]

In the present study, a novel metal nanostructure of Ag@SiO_2@Lu_2O_3:Gd/Yb/Er was fabricated and its property was investigated. An upconversion emission enhancement of 30-fold was obtained, which is greater than those reported in our previous works and some papers.[26,33−35] The as-prepared nanocomposite exhibited bright fluorescence when it was used for imaging with HeLa cells. All the results showed that the as-prepared nanocomposite is a potential nano fluorescent probe that can be applied in highly sensitive bioimaging and detection.

2. EXPERIMENTAL SECTION

2.1. Materials. Rare earth oxides Lu_2O_3 (99.999%), Yb_2O_3 (99.999%), Gd_2O_3 (99.999%), and Er_2O_3 (99.999%) were purchased from Shanghai Yuelong New Materials Co. Ltd. Poly(oxyethylene) nonylphenyl ether (Igepal CO-520) and polyvinylpyrrolidone (PVP) were purchased from Sigma-Aldrich. Silver nitrate ($AgNO_3$), phosphate buffered saline (PBS), tetraethoxysilane (TEOS), ethylene glycol, urea, ammonia solution (28 wt %), ethanol, acetone, and cyclohexane were purchased from Enterprise Group Chemical Reagent Co., Ltd. (Shanghai). $LnCl_3$ (Ln = Lu, Gd, Yb, Er) was prepared by dissolving the corresponding metal oxide in hydrochloric acid at elevated temperature. All other reagents were of analytical grade and were used directly without further purification.

2.2. Synthesis of Silver Nanoparticles. PVP (10 g) was dissolved in 75 mL of ethylene glycol at room temperature; then, 400 mg of $AgNO_3$ was added to this solution with continuous stirring. The suspension was stirred at room temperature until $AgNO_3$ was dissolved completely. Then, the mixture was heated up to 120 °C at a constant rate of 1 °C/min and kept at this temperature for 1 h. At the end of the reaction period, the colloidal dispersion was cooled down to room temperature. The desired silver nanoparticles were obtained by adding a large amount of acetone and then centrifugation at 8000 rpm for 10 min.

2.3. Synthesis of Ag@SiO_2 Core−Shell Nanoparticles. The core−shell Ag@SiO_2 nanoparticles were prepared by a facile reverse microemulsion method. Briefly, the water-in-oil (W/O) reverse microemulsion was formed at room temperature in a 30 mL three-neck flask containing 4 mL of Igepal CO-520, 10 mL of cyclohexane, 2 mL of water, and 0.15 g of as-prepared silver nanoparticles under vigorous stirring. After 20 min, 50 μL of ammonia was added as a catalyst. After the equilibration period (25 min), 100 μL of a stock solution of TEOS containing 50% TEOS and 50% cyclohexane by weight was injected into the microemulsion to initiate the polymerization reaction. After stirring for 48 h, the resulting core−shell nanoparticles were isolated from the microemulsion by adding an appropriate amount of acetone, followed by centrifuging and washing with ethanol and water for several times.

2.4. Synthesis of Ag@SiO_2@Lu_2O_3:Gd/Yb/Er Nanocomposite. Typically, 2.2 g of urea and 0.75 mmol of $LnCl_3$ (Ln = 54% Lu, 24% Gd, 20% Yb, 2% Er) were dissolved in 200 mL of deionized water. As-prepared Ag@SiO_2 nanoparticles (0.05 g) were dispersed in the solution with continuous stirring for 20 min. The suspension was sealed in a bottle and heated to 90 °C for 2 h with stirring. After cooling down to room temperature, particles were separated by centrifugation and then washed with ethanol and water for several times. The obtained precursor was dried and calcined at 700 °C for 2 h (heating rate: 2 °C/min) to obtain the final product (Ag@SiO_2@Lu_2O_3:Gd,Yb,Er nanocomposite).

2.5. Measurement of Upconversion Absolute Quantum Yield. According to the method reported by van Veggel, Zhang, and co-workers,[36,37] the fluorescence spectrophotometer (Edinburgh FLS920) was modified by using an Ocean Optics UV−vis−NIR CCD (QE65000) as a detector for detection of the excitation light from a continuous-wave 980 nm laser and upconversion emission. An integrating sphere was also used to measure the efficiency data. The response of the detection systems in photon flux was determined using a calibrated VIS-NIR lamp (Ocean Optics LS-1-CAL). The quantum yield of the upconversion luminescence of the nanocrystals was calculated using the following equation

$$\mathrm{QY} = \frac{\text{Photons emitted}}{\text{Photons absorbed}} = \frac{L_{\text{sample}}}{E_{\text{blank}} - E_{\text{sample}}}$$

where QY is the quantum yield, L_{sample} is the emission intensity, and E_{blank} and E_{sample} are the intensities of the excitation light in the absence and presence of the upconversion nanocrystal samples, respectively.

2.6. Bioapplication of the Nanocomposite for HeLa Cell Imaging. The confocal UCL imaging of HeLa cells with the prepared nanocomposite was carried out as reported previously.[38] Typically, HeLa cells were grown in the MEM (Modified Eagle's Medium) supplemented with 10% FBS (fetal bovine serum) at 37 °C and 5% CO_2. Cells (5×10^8/L) were plated on 14 mm (diameter) glass coverslips and allowed to adhere for 24 h. Before the imaging experiments, HeLa cells were washed with PBS (pH = 7) and then incubated with the nanocomposite (200 μg/mL) at 37 °C for 3 h. Cell imaging was performed with a laser scanning upconversion luminescence microscope.

2.7. Cytotoxicity Assay. Cell viability was measured using the MTT [3-(4,5-dimethylthiazol-2-yl)-2,5-diphenyltetrazolium bromide] assay. Briefly, HeLa cells were seeded in a 96-well flat-bottom microplate (2×10^4 cells per well) and cultured in 100 μL of growth media at 37 °C and 5% CO_2 for 12 h. The cell culture medium in each well was then replaced by 100 μL of cell growth medium containing Ag@SiO_2@Lu_2O_3:Gd,Yb,Er with the concentrations ranging from 100 to 1000 μg/mL. After incubation for 24 h, 100 μL of MTT (0.5 mg/mL in PBS) was added to each well for further incubation at 37 °C for 4 h. The growth media were removed gently by suction. Then, 150 μL of DMSO was added to every well as solubilizing agent, and the microplates were left at room temperature for 2 h. Absorbance at 490 nm was measured on a Microplate Reader (BIO-RAD Corporation), and each data point was presented as mean ± standard deviation (SD) from sextuplicate wells.

2.8. Characterizations. The sizes and morphologies of nanocrystals were characterized with a JEOL JEM-2010F transmission electron microscope (TEM) operating at 200 kV. Energy-dispersive X-ray analysis (EDX) of the samples was performed during high-resolution transmission electron microscopy (HRTEM) measurements to determine the elements of the samples. The crystal phase structures of the as-prepared samples were examined by powder X-ray diffraction (XRD) measurements that were performed on a Rigaku D/max-2500 X-ray diffractometer using Cu Kα radiation. The scan was performed in the 2θ range from 10° to 80° with a scanning rate of 8°/min. The upconversion luminescence spectra were recorded with an Edinburgh FLS-920 fluorescence spectrophotometer using an external 0−2 W adjustable laser (980 nm, Beijing Hi-Tech Optoelectronic Co., China) as the excitation source instead of the xenon source in the spectrophotometer. The images of upconversion luminescence were obtained digitally with a Nikon multiple CCD camera. Time-resolved spectra and upconversion luminescence lifetimes were measured with a customized phosphorescence lifetime spectrometer (FSP920-C, Edinburgh) equipped with a digital oscilloscope and a tunable midband OPO pulse laser as excitation source (410−2400 nm, 10 Hz, pulse width ≤ 5 ns, Vibrant 355II, OPOTEK). All the photoluminescence studies were carried out at room temperature.

3. RESULTS AND DISCUSSION

3.1. Structure, Morphology, and Composition of the Nanocomposite. The stepwise preparation of the Ag@SiO_2@Lu_2O_3:Gd/Yb/Er nanostructure is shown in Figure 1. First, water-soluble silver nanoparticles were prepared by heating $AgNO_3$ and ethylene glycol in the presence of PVP. Then, the Ag nanoparticles were coated with a silica layer to obtain the Ag@SiO_2 composite through a facile reverse microemulsion method. The grain diameters of the Ag core and silica thickness were controlled by changing the concentrations of $AgNO_3$ and

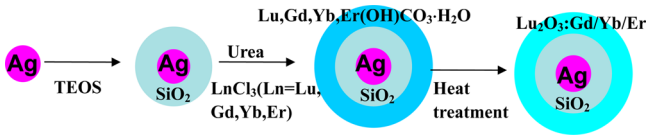

Figure 1. Synthetic procedure of the $Ag@SiO_2@Lu_2O_3$:Gd/Yb/Er nanostructure.

silica precursor, respectively. Then, the formed $Ag@SiO_2$ nanoparticles were all coated with a layer of Lu,Gd,Yb,Er-$(OH)CO_3·H_2O$ through a homogeneous precipitation method in an aqueous solution of lanthanide (Lu, Gd, Yb, Er) chlorides and urea at 90 °C for 2 h. Finally, the amorphous $Lu,Gd,Yb,Er(OH)CO_3·H_2O$ layer was transformed into cubic phase Lu_2O_3:Gd/Yb/Er after heat treatment at 700 °C for 2 h.

The XRD patterns of the prepared products are shown in Figure 2. Both of $SiO_2@Lu_2O_3$:Gd/Yb/Er and $Ag@SiO_2@$

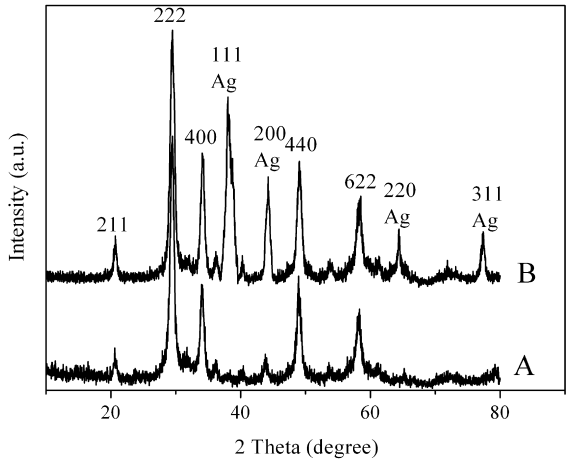

Figure 2. XRD patterns of $SiO_2@Lu_2O_3$:Gd/Yb/Er (A) and $Ag@SiO_2@Lu_2O_3$:Gd/Yb/Er (B).

Lu_2O_3:Gd/Yb/Er showed the same characteristic diffraction peaks (211, 222, 400, 440, and 622), which can be indexed as a typical cubic crystalline phase of Lu_2O_3 (JCPDS 12-0728). $Ag@SiO_2@Lu_2O_3$:Gd/Yb/Er showed four well-resolved diffraction peaks of 111, 200, 220, and 311, which can be indexed as a typical face-centered cubic phase of silver (JCPDS 87-0720) and were absent in $SiO_2@Lu_2O_3$:Gd/Yb/Er.

Figure 3 shows the TEM and HRTEM images of the $Ag@SiO_2$ and $Ag@SiO_2@Lu_2O_3$:Gd/Yb/Er nanoparticles. $Ag@SiO_2$ showed a core−shell structure with a dark contrast silver core (~20 nm) and a light contrast silica shell (~30 nm). The average size of the nanoparticles was about 80 nm. Figure 3B shows that $Ag@SiO_2@Lu_2O_3$:Gd/Yb/Er had a core−shell structure and each of the particles had one silver core (~20 nm) and two shells consisting of a light silica shell (~30 nm) and a dark Lu_2O_3 shell (~4 nm). The average grain diameter of the particles was about 88 nm. Compared to $Ag@SiO_2$, the increase in the size could be attributed to a coated Lu_2O_3 shell. As the control, a $SiO_2@Lu_2O_3$:Gd/Yb/Er nanocomposite was prepared using the similar synthetic procedure to $Ag@SiO_2@Lu_2O_3$:Gd/Yb/Er, except the replacement of $Ag@SiO_2$ nanoparticles with SiO_2 nanoparticles with the same size. Figure S3 (Supporting Information) shows that the $SiO_2@Lu_2O_3$:Gd/Yb/Er nanocomposite displayed a similar morphology and size to those of $Ag@SiO_2@Lu_2O_3$:Gd/Yb/Er with a similar thickness of the Lu_2O_3 shell, although it had no Ag core. The HRTEM image of Ag core (Figure 3A, inset) shows that the value of the interplanar distance between adjacent lattice fringes was determined as about 0.24 nm, which was assigned to the {111} crystal plane of the cubic (fcc) silver.[39] The HRTEM image of the Lu_2O_3 layer (Figure 3B, inset) reveals a distance of 0.319 nm of the crystal fringes, which was assigned to the {222} crystal plane of the Lu_2O_3 bcc phase.[40] This confirmed the formation of a Lu_2O_3 layer on the silica shell. The results of TEM images and XRD patterns were in good agreement, confirming that the core−shell structure of the $Ag@SiO_2@Lu_2O_3$:Gd,Yb,Er nanocomposite was fabricated successfully. The composition of the nanocomposite was characterized by EDX analysis. As shown in Figure 4, almost all of the elements, including Ag, Si, O, Lu, Gd, and Yb, could be detected, further confirming the formation of the nanocomposite.

3.2. UV−vis Absorption Spectra and Upconversion Luminescence Property of the Nanocomposite. Figure 5 shows the UV−vis absorption spectra of $Ag@SiO_2$, $SiO_2@Lu_2O_3$:Gd/Yb/Er, and $Ag@SiO_2@Lu_2O_3$:Gd/Yb/Er nanoparticles. $Ag@SiO_2$ showed the well-known surface phasmon resonance (SPR) band at 350−665 nm, which was similar to the value reported in the literature.[41] $Ag@SiO_2@Lu_2O_3$:Gd/Yb/Er displayed a broad absorption band of SPR and the SPR peak shift toward a longer wavelength owing to the change of local refractive index around the Ag particles caused by the shells of Lu_2O_3:Gd/Yb/Er. As the control, $SiO_2@Lu_2O_3$:Gd/Yb/Er showed no SPR peaks, further confirming that the silver core had successfully formed in the nanocomposite.

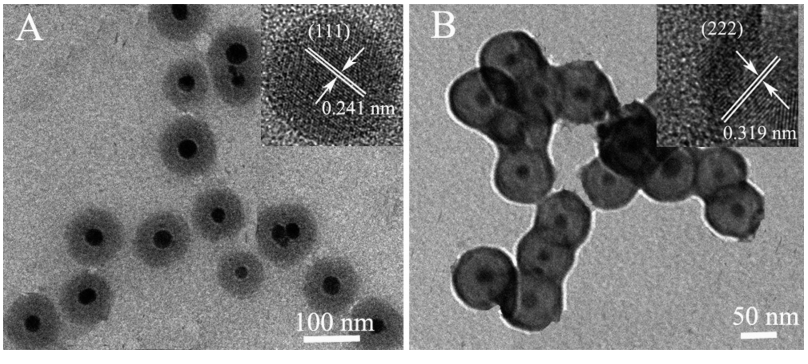

Figure 3. TEM images of $Ag@SiO_2$ (A) and $Ag@SiO_2@Lu_2O_3$:Gd/Yb/Er (B) nanoparticles, and HRTEM images of Ag (A, inset) and Lu_2O_3 (B, inset).

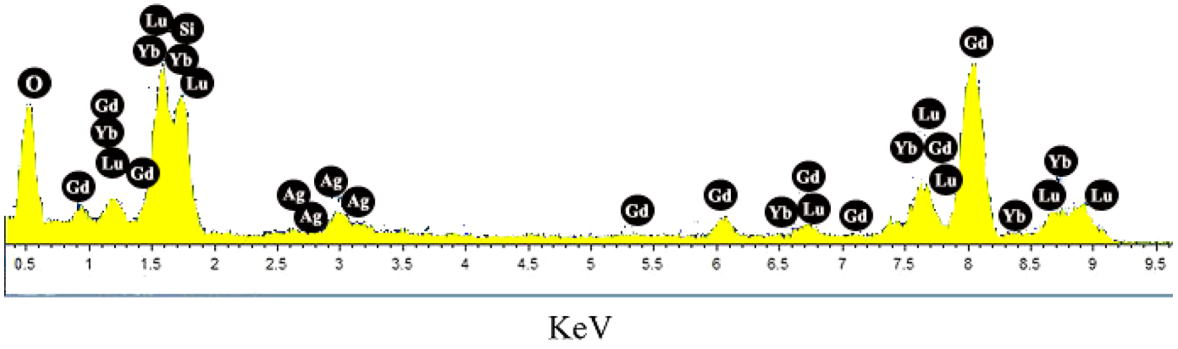

Figure 4. EDX analysis of elemental composition of $Ag@SiO_2@Lu_2O_3$:Gd/Yb/Er.

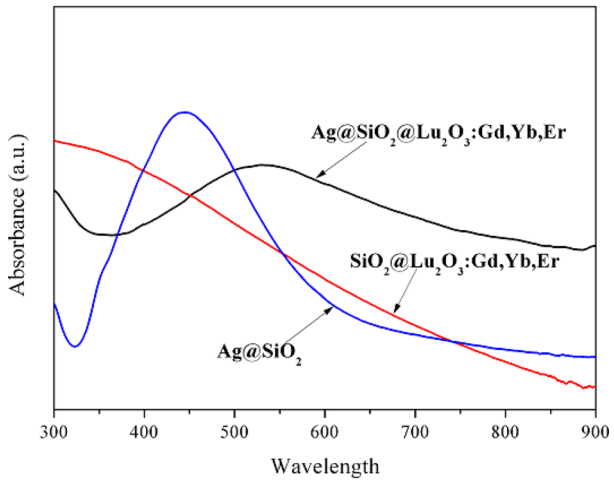

Figure 5. UV−vis absorption spectra of $Ag@SiO_2$, $SiO_2@Lu_2O_3$:Gd/Yb/Er, and $Ag@SiO_2@Lu_2O_3$:Gd/Yb/Er nanoparticles.

The upconversion luminescence spectra of $SiO_2@Lu_2O_3$:Gd/Yb/Er and $Ag@SiO_2@Lu_2O_3$:Gd/Yb/Er nanoparticles were measured at the same concentrations of 1.0 mg/mL in aqueous solutions with excitation at 980 nm. As shown in Figure 6, both of them showed identical characteristic emission

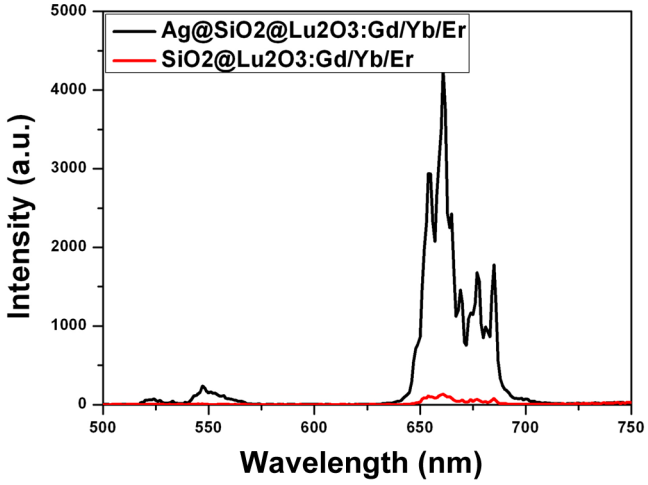

Figure 6. Upconversion luminescence spectra of $SiO_2@Lu_2O_3$:Gd/Yb/Er (A) and $Ag@SiO_2@Lu_2O_3$:Gd/Yb/Er (B) nanocomposites under excitation at a CW 980 nm laser.

peaks of Er^{3+} with strong red emission peaks near 662 nm corresponding to the $^4F_{9/2} \rightarrow {}^4I_{15/2}$ transition and very weak emissions near 520 and 550 nm corresponding to the $^2H_{11/2} \rightarrow {}^4I_{15/2}$ and $^4S_{3/2} \rightarrow {}^4I_{15/2}$ transitions, respectively.[26,40] This emission feature was similar to that observed with other Er^{3+}-doped oxide nanocrystals.[40,42,43] Such upconversion luminescence with strong red light and weak short-wavelength light favors in vivo imaging, since short-wavelength light can be absorbed by tissues with lower penetration, whereas red light can penetrate tissue deeply and minimize absorption and autofluorescence of tissues.[44,45]

It was interesting to find that the $Ag@SiO_2@Lu_2O_3$:Gd/Yb/Er nanocomposite showed a high fluorescence enhancement (30-fold) compared to the control of silver-free nanocomposite ($SiO_2@Lu_2O_3$:Gd/Yb/Er), as shown in Figure 6. This enhancement was attributed to the MEF, which arises from the interaction of the fluorophore and surface plasmon resonance of metal nanoparticles. Surface plasmon resonance (SPR) is the collective electron-cloud oscillation on a metal surface or nanoparticles and is caused by the interaction of the metal with incident light.[46,47] A key aspect of the SPR effect is the associated increase in the intensity of the local electric field in the proximity of nanoparticles, which can significantly modify the spectroscopic properties of neighboring fluouophores.[48]

The theory of MEF has been developed since the 1980s,[49] in which the effects are attributed to at least three known mechanisms (Figure S1, Supporting Information).[49,52] One is energy transfer quenching, k_m, to the metal with a d^{-3} dependence.[49] This quenching can be understood by damping of the dipole oscillations by the nearby metal. A second mechanism is an increase in the emission intensity as a result of the SPR increasing the local electric field on the fluorophore, E_m. This effect will result in increased intensities, but the lifetime and quantum yield of the fluorophore will be unchanged. This fluorescent enhancement can be understood as being due to the metal particles that concentrate the local electric field and subsequently increase the rate of excitation.[50] The maximum enhancement of fluorescence emission is achieved if the SPR wavelength equals the absorption wavelength of fluorophores.[50] The third mechanism is that a nearby metal can increase the intrinsic radiative decay rate of the fluorophore, Γ_m, resulting in increasing quantum yield and emission intensity of the fluorophore.[51] The maximum enhancement of fluorescence emission is achieved if the SPR wavelength equals the emission wavelength of fluorophores.[23]

To better understand this mechanism, it is informative to consider the Jablonski diagram for fluorophores in the free-space condition and the modified form when they are in close proximity to conducting metallic particles (Figure S2, Supporting Information).[52,53]

The quantum yield (Q) and lifetime (τ) of a fluorophore are given by

$$Q = \frac{\Gamma}{\Gamma + k_{nr}}$$

$$\tau = \frac{1}{\Gamma + k_{nr}}$$

where Γ is the intrinsic radiative or emissive rate and k_{nr} represents the nonradiative decay rate.

Let Γ_m represent the rate of the radiative decay due to the presence of the metal particles. This new rate changes the quantum yield to

$$Q_m = \frac{\Gamma + \Gamma_m}{\Gamma + \Gamma_m + k_{nr}}$$

The lifetime in the presence of metal will be decreased to

$$\tau_m = \frac{1}{\Gamma + \Gamma_m + k_{nr}}$$

Hence, an increase in the radiative decay rate of a fluorophore can explain both the increased emission intensity and the decreased lifetime in the presence of metal particles.

We proposed that the observed upconversion emission enhancement of 30-fold in the present study may be attributed to at least two possible factors: (1) an increase in the excitation rate by local electric field enhancement, that is, an enhancement of the effective excitation flux caused by the local electric field enhancement associated with SPR; and (2) an increase in the radiative decay rate of the fluorophore by surface plasmon-coupled emission (SPCE), that is, an enhancement of emission efficiency because of the coupling of the unconversion emission with the NPs plasmonic resonance, which will effectively increase the radiative decay rate. SPCE can occur when the emission band of the fluorophore overlaps with the plasmon resonance frequency of the metal nanostructures.[52] Both of the factors have been used to explain the MEF in quantum dots or fluorescent molecules.[51,54]

It can be seen in Figure 5 (UV−vis spectra of Ag@SiO_2@Lu_2O_3:Gd/Yb/Er) and Figure 6. In our case, the SPR absorption band of Ag nanoparticles did not overlap with the excitation wavelength (980 nm) of the UCNs, but overlapped with the emission bands of UCNs (550 and 662 nm). Therefore, the SPR of Ag NPs could effectively couple with the upconversion emission and could thus increase the radiative decay rate, emission efficiency, and intensity of the nanocomposite. With a better plasmonic coupling near the plasmon resonance frequency, the SPCE was also a reason why the observed enhancement factor (40) was larger for green emission (550 nm) than for red emission (Figure 6). This suggested that the SPCE played an important role in the spectra-dependent enhancement of upconversion emission, although other effects such as local electric field enhancement might also contribute to the enhancement. Thus, the emission enhancement in this case could be dominantly attributed to the increase in the radiative decay rate by the SPCE.

In order to verify the proposed enhancement mechanism, time-resolved spectra and UCL lifetimes were measured for nanocomposites with and without the Ag core (Figure S3, Supporting Information). The measured values of lifetimes for these materials are 150.4 and 302.2 μs, respectively. Obviously, the lifetime of Ag@SiO_2@Lu_2O_3:Gd/Yb/Er was lower than that of SiO_2@Lu_2O_3:Gd/Yb/Er. These results demonstrated that the lifetime of the nanocomposite reduced when the composite contained a Ag core. For SiO_2@Lu_2O_3:Gd/Yb/Er and Ag@SiO_2@Lu_2O_3:Gd/Yb/Er, the measured lifetimes $\tau(1/(\Gamma + k_{nr}))$ were 302.2 and 150.4 μs for the emission peak at 660 nm, respectively. Their measured quantum yields Q $(\Gamma/\Gamma + k_{nr})$ were 0.03% and 0.61%, respectively. From the measured lifetimes and quantum yields, we estimated Γ = 0.993 and 40.56 s^{-1} for SiO_2@Lu_2O_3:Gd/Yb/Er and Ag@SiO_2@Lu_2O_3:Gd/Yb/Er, respectively. The increased radiative decay rate is consistent with the UCL enhancement measured experimentally and consistent with the measured changes in lifetime.

Hence, an increase in the radiative decay rate by the metal could explain both the increased fluorescence intensity and the decreased lifetime in the presence of the Ag core. These results were consistent with the above mechanism that the fluorescence enhancement was dominantly attributed to the increase in the radiative decay rate caused by the MEF (SPCE).

It was worth noting that the upconversion luminescence enhancement of 30-fold caused by the MEF was a rather great value in comparison with those reported in our previous works and other studies,[26,31,35] indicating that the fluorophore was an important factor to achieve the greatest enhancement of emission. Of course, the separation distance between the Ag nanoparticles and fluorophores, and the size of the Ag nanoparticles, also played important roles in the MEF. In our case, the separation distance controlled by the silica shell thickness and the size of the Ag core controlled by the $AgNO_3$ concentration were chosen as 30 and 20 nm, respectively, based on the data reported in the literature with some rational modifications.[26,31,33]

The measured absolute UCL quantum yield of the Ag@SiO_2@Lu_2O_3:Gd/Yb/Er nanocomposite was 0.62 ± 0.1%, which was higher than those reported in the literature.[36−38] Such a nanocomposite displayed strong UCL with a rather high quantum yield, indicating that the prepared Ag@SiO_2@Lu_2O_3:Gd/Yb/Er was an excellent upconversion luminescent material.

Considering that the MEF is dependent on many factors, such as metal nanoparticle size, shape, and metal−fluorophore distance, we prepared various Ag@SiO_2@Lu_2O_3:Gd/Yb/Er nanocomposites with variant Ag cores (Figure S5, Supporting Information) and silica shells (Figure S6, Supporting Information) and investigated their upconversion luminescence properties. The results revealed that the MEF effect depended sensitively on the sizes of Ag cores and thickness of silica shells. The UCL was quenched (enhancement factors < 1) with a thin SiO_2 spacer. This could be attributed to that the close proximity of the Ag sphere with the shell caused efficient nonradiative energy transfer from the UCNs to the metallic surface. With increasing spacer thickness, the average UCL intensity reached a maximum value at an optimal spacer thickness of 30 nm, and then decreased with the increase in the spacer thickness. This phenomenon was well consistent with recent reports.[26,32,55] With an increase in the Ag core size from 25 to 100 nm, the UCL of the nanocomposite increased in the beginning and reached a maximum value at an optimal Ag core size of 75 nm, and then decreased when the Ag core increased to 100 nm. The

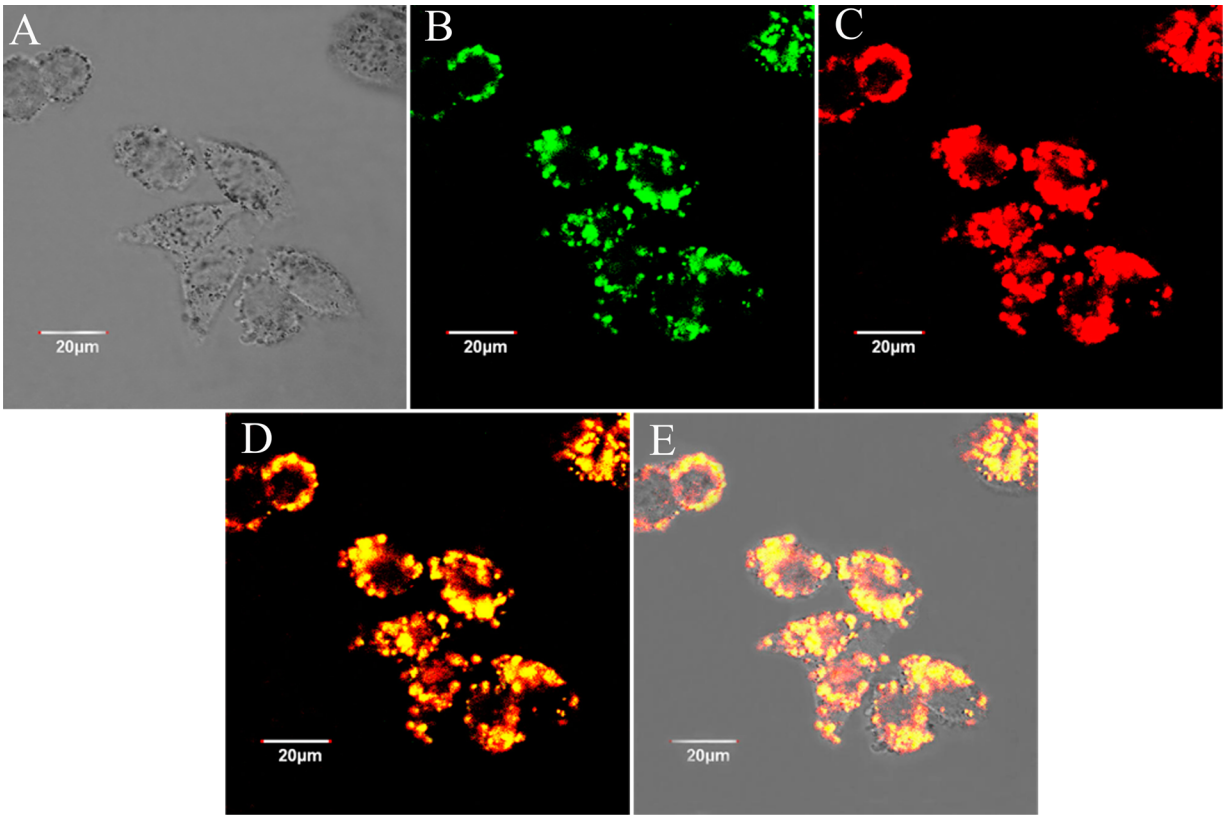

Figure 7. Bright-field image of HeLa cells (A), confocal images of HeLa cells after incubation with the nanocomposite, collected at green (520−560 nm) (B) and red (625−700 nm) channels (C), the merged image of panels B and C (D), and the merged image of the bright-field one and panels B and C (E).

real reason for this phenomenon was not clear and needed to be further investigated. We assumed that the enhancement of local electric field depended on the Ag core size and the large Ag core could cause a great enhancement, leading to high excitation efficiency and emission intensity. However, the Ag core with the size being too large could cause the shifting of the SPR peak to the near-infrared region and reduced the SPCE, and also significantly increased the scattering of excitation light at 980 nm. Thus, the effective excitation flux was reduced, which led to a quench of the UCL.[27]

3.3. HeLa Cell Imaging Using the Nanocomposite. To examine the potential of the nanocomposite for bioimaging, a cellular imaging experiment using the nanocomposite and HeLa cells was performed with a laser scanning upconversion luminescence microscope under CW excitation at 980 nm. The cellular uptake of the nanocomposite was carried out by incubating HeLa cells with 200 μg/mL of the nanocomposite in PBS (pH = 7) at 37 °C for 3 h. The images were obtained using a confocal microscopy. As shown in Figure 7, intense luminescence signals at 625−700 nm (red light) and 520−560 nm (green light) were detected in the cytoplasm regions. A quantitative analysis of the intensities of the UCL signal and the background was made to present the UCL signal ratio for the living cells labeled with the nanocomposite (Figure 8). Five points were selected for analysis of the signal ratio of the UCL images. The luminescence intensity profile of HeLa cells revealed an extremely high signal ratio in the cytoplasm (counts ~ 4000 for region 2 and region 4) and no background luminescence in the nucleus (counts ~ 0 for region 3), suggesting an exclusive staining of the cytoplasm.

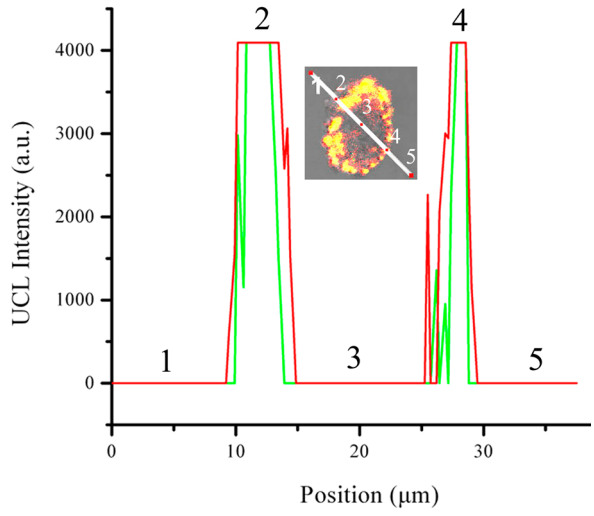

Figure 8. Upconversion luminescence intensities corresponding to the extracellular region (1 and 5), cytoplasm (2 and 4), and nuclear region (3).

Three-dimensional (3D) imaging of live cells was also performed (Figure 9). HeLa cells were loaded with the nanocomposite and then were imaged by serially scanning at increasing depths along the *z* axis. As shown in an *xy* image of the cells obtained at a certain depth of *z*, the cytoplasms of HeLa cells were perfectly visualized in the *xz* and *yz* cross-sectional images, indicating that the nanocomposite was internalized in the cytoplasms and emited upconversion luminescence in the cytoplasm regions.

dx.doi.org/10.1021/am505633g | ACS Appl. Mater. Interfaces 2014, 6, 18480−18488

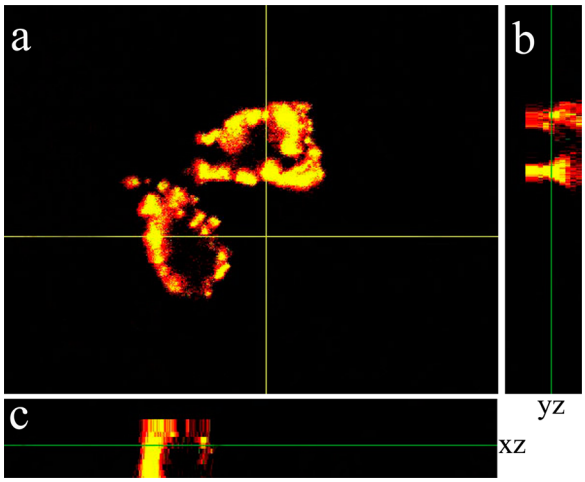

Figure 9. Three-dimensional luminescence images of Hela cells: Panel a was an *xy* image, while panels b and c displayed the *yz* and *xz* cross sections taken at the lines shown in panel a, respectively.

3.4. Cytotoxicity Test. Toxicity is a critical factor for determining the feasibility of the as-prepared nanoparticles in bioimaging applications. The viability of HeLa cells after exposure to Ag@SiO_2@Lu_2O_3:Gd/Yb/Er UCNs with different concentrations was measured by a standard MTT assay. As shown in Figure S7 (Supporting Information), the prepared UCNs showed negligible cytoxicity toward HeLa cells, even at a high dose of 1000 μg/mL for 24 h (viability > 90%). The high viability of cells showed the good biocompatibility and the potential of the UCNs for bioimaging applications.

4. CONCLUSIONS

In summary, a novel core−shell nanocomposite Ag@SiO_2@Lu_2O_3:Gd/Yb/Er has been developed successfully. The MEF for the upconversion nanocrystal Lu_2O_3:Gd/Yb/Er and the HeLa cells imaging with the nanocomposite were investigated. The results showed that a 30-fold MEF factor was observed. This enhancement could be dominantly attributed to the increase in the radiative decay rate and emission efficiency caused by the SPCE. The cell imaging experiments revealed that the nanocomposite could enter the cytoplasm through cellular cytophagocytosis and cause the cells to exhibit strong upconversion fluorescence. The characterized properties and cell imaging application of the prepared nanocomposite showed that the nanocomposite had potential to be used as a fluorescent probe for highly sensitive biological, medical, and optical detections.

■ ASSOCIATED CONTENT

Supporting Information

The diagram of MEF mechanisms, classical Jablonski diagram, time-resolved spectra of Ag@SiO_2@Lu_2O_3:Gd/Yb/Er and SiO_2@Lu_2O_3:Gd/Yb/Er, TEM images of SiO_2@Lu_2O_3:Gd/Yb/Er nanocomposites, TEM images of Ag@SiO_2 and Ag@SiO_2@Lu_2O_3:Gd/Yb/Er with variant Ag cores and silica shells, and viability of HeLa cells incubated with different concentrations of Ag@SiO_2@Lu_2O_3:Gd/Yb/Er for 24 h. This material is available free of charge via the Internet at http://pubs.acs.org.

■ AUTHOR INFORMATION

Corresponding Authors

*E-mail: ydg@shu.edu.cn (D.Y.).

*E-mail: mhwu@shu.edu.cn (M.W.).

Notes

The authors declare no competing financial interest.

■ ACKNOWLEDGMENTS

The authors acknowledge the National Natural Science Foundation of China (Nos. 21271126, 11025526), the National 973 Program (No. 2010CB933901), and the Program for Changjiang Scholars and Innovative Research Team in University (No. IRT 13078).

■ REFERENCES

(1) Suyver, J.; Aebischer, A.; Biner, D.; Gerner, P.; Grimm, J.; Heer, S.; Krämer, K.; Reinhard, C.; Güdel, H. Novel Materials Doped with Trivalent Lanthanides and Transition Metal Ions Showing Near-Infrared to Visible Photon Upconversion. *Opt. Mater.* **2005**, *27*, 1111−1130.

(2) Zhou, J.; Liu, Z.; Li, F. Y. Upconversion Nanophosphors for Small-Animal Imaging. *Chem. Soc. Rev.* **2012**, *41*, 1323−1349.

(3) Wang, F.; Deng, R. R.; Wang, J.; Wang, Q. X.; Han, Y.; Zhu, H. M.; Chen, X. Y.; Liu, X. G. Tuning Upconversion through Energy Migration in Core-Shell Nanoparticles. *Nat. Mater.* **2011**, *10*, 968−973.

(4) Wang, F.; Han, Y.; Lim, C. S.; Lu, Y. H.; Wang, J.; Xu, J.; Chen, H. Y.; Zhang, C.; Hong, M. H.; Liu, X. G. Simultaneous Phase and Size Control of Upconversion Nanocrystals through Lanthanide Doping. *Nature* **2010**, *463*, 1061−1065.

(5) Zhou, J.; Yu, M.; Sun, Y.; Zhang, X.; Zhu, X.; Wu, Z.; Wu, D.; Li, F. Y. Fluorine-18-Labeled $Gd^{3+}/Yb^{3+}/E^{r3+}$ Co-doped $NaYF_4$ Nanophosphors for Multimodality PET/MR/UCL Imaging. *Biomaterials* **2011**, *32*, 1148−1156.

(6) Saboktakin, M.; Ye, X. C.; Oh, S. J.; Hong, S. H.; Fafarman, A. T.; Chettiar, U. K.; Engheta, N.; Murray, C. B.; Kagan, C. R. Metal-Enhanced Upconversion Luminescence Tunable through Metal Nanoparticle−Nanophosphor Separation. *ACS Nano* **2012**, *6*, 8758−8766.

(7) Ye, X. C.; Collinsb, J. E.; Kanga, Y. J.; Chenc, J.; Chend, D. T. N.; Yodhd, A. G.; Murraya, C. B. Morphologically Controlled Synthesis of Colloidal Upconversion Nanophosphors and Their Shape-Directed Self-Assembly. *Proc. Natl. Acad. Sci. U.S.A.* **2010**, *107*, 22430−22435.

(8) Liu, Q.; Sun, Y.; Yang, T. S.; Feng, W.; Li, C. G.; Li, F. Y. Sub-10 nm Hexagonal Lanthanide-Doped $NaLuF_4$ Upconversion Nanocrystals for Sensitive Bioimaging in Vivo. *J. Am. Chem. Soc.* **2011**, *133*, 17122−17125.

(9) Yu, M. X.; Li, F. Y.; Chen, Z. G.; Hu, H.; Zhan, C.; Yang, H.; Huang, C. H. Laser Scanning Up-Conversion Luminescence Microscopy for Imaging Cells Labeled with Rare-Earth Nanophosphors. *Anal. Chem.* **2009**, *81*, 930−935.

(10) Liu, Q.; Feng, W.; Yang, T. S.; Yi, T.; Li, F. Y. Upconversion Luminescence Imaging of Cells and Small Animals. *Nat. Protoc.* **2013**, *8*, 2033−2044.

(11) Pichaandi, J.; Boyer, J. C.; Delaney, K. R.; Van Veggel, F. C. Two-Photon Upconversion Laser (Scanning and Wide-Field) Microscopy Using Ln(3+)-Doped $NaYF_4$ Upconverting Nanocrystals: A Critical Evaluation of their Performance and Potential in Bioimaging. *J. Phys. Chem. C* **2011**, *115*, 19054−19064.

(12) Feng, W.; Sun, D. L.; Yan, H. C. Ag Nanowires Enhanced Upconversion Emission of $NaYF_4$: Yb, Er Nanocrystals via a Direct Assembly Method. *Chem. Commun.* **2009**, *29*, 4393−4395.

(13) Yi, S. G.; Chow, M. G. Water-Soluble $NaYF_4$:Yb, Er (Tm)/$NaYF_4$/Polymer Core/Shell/Shell Nanoparticles with Significant Enhancement of Upconversion Fluorescence. *Chem. Mater.* **2007**, *19*, 341−343.

(14) Boyer, J. C.; Manseau, M. P.; Murray, J. I.; Van Veggel, F. C. Surface Modification of Upconverting $NaYF_4$ Nanoparticles with PEG-Phosphate Ligands for NIR (800 nm) Biolabeling within the Biological Window. *Langmuir* **2009**, *26*, 1157−1164.

(15) Cheng, L.; Yang, K.; Zhang, S.; Shao, M.; Lee, S.; Liu, Z. Highly-Sensitive Multiplexed in Vivo Imaging Using PEGylated Upconversion Nanoparticles. *Nano. Res.* **2010**, *3*, 722−732.
(16) Zhang, J.; Mi, C.; Wu, H.; Huang, H.; Mao, C.; Xu, S. Synthesis of $NaYF_4$:Yb/Er/Gd Up-Conversion Luminescent Nanoparticles and Luminescence Resonance Energy Transfer-Based Protein Detection. *Anal. Biochem.* **2012**, *421*, 673−679.
(17) Kumar, R.; Nyk, M.; Ohulchanskyy, T. Y.; Flask, C. A.; Prasad, P. N. Combined Optical and MR Bioimaging Using Rare Earth Ion Doped $NaYF_4$ Nanocrystals. *Adv. Funct. Mater.* **2009**, *19*, 853−859.
(18) Chen, G.; Ohulchanskyy, T. Y.; Liu, S.; Law, W. C.; Wu, F.; Swihart, M. T.; Ågren, H.; Prasad, P. N. Core/Shell $NaGdF_4$:Nd^{3+}/$NaGdF_4$ Nanocrystals with Efficient Near-Infrared to Near-Infrared Downconversion Photoluminescence for Bioimaging Applications. *Acs. Nano* **2012**, *6*, 2969−2977.
(19) Jiang, T.; Liu, Y.; Liu, S.; Liu, N.; Qin, W. Upconversion Emission Enhancement of Gd^{3+} Ions Induced by Surface Plasmon Field in Au@ $NaYF_4$ Nanostructures Codoped with Gd^{3+}-Yb^{3+}-Tm^{3+} Ions. *J. Colloid Interface Sci.* **2012**, *377*, 81−87.
(20) Dubertret, B.; Calame, M.; Libchaber, A. J. Single-Mismatch Detection Using Gold-Quenched Fluorescent Oligonucleotides. *Nat. Biotechnol.* **2001**, *19*, 365−370.
(21) Aslan, K.; Leonenko, Z.; Lakowicz, J. R.; Geddes, C. D. Fast and Slow Deposition of Silver Nanorods on Planar Surfaces: Application to Metal-Enhanced Fluorescence. *J. Phys. Chem. B* **2005**, *109*, 3157−3162.
(22) Aslan, K.; Wu, M.; Lakowicz, J. R.; Geddes, C. D. Fluorescent Core−Shell Ag@ SiO_2 Nanocomposites for Metal-Enhanced Fluorescence and Single Nanoparticle Sensing Platforms. *J. Am. Chem. Soc.* **2007**, *129*, 1524−1525.
(23) Lakowicz, J. R.; Shen, B.; Gryczynski, Z.; D'Auria, S.; Gryczynski, I. Intrinsic Fluorescence from DNA Can Be Enhanced by Metallic Particles. *Biochem. Biophys. Res. Commun.* **2001**, *286*, 875−879.
(24) Mertens, H.; Polman, A. Plasmon-Enhanced Erbium Luminescence. *Appl. Phys. Lett.* **2006**, *89*, 211107.
(25) Som, T.; Karmakar, B. Nanosilver Enhanced Upconversion Fluorescence of Erbium Ions in Er^{3+}:Ag-Antimony Glass Nanocomposites. *J. Appl. Phys.* **2009**, *105*, 013102.
(26) Zhang, F.; Braun, G. B.; Shi, Y.; Zhang, Y.; Sun, X.; Reich, N. O.; Zhao, D.; Stucky, G. Fabrication of Ag@ SiO_2@Y_2O_3:Er Nanostructures for Bioimaging: Tuning of the Upconversion Fluorescence with Silver Nanoparticles. *J. Am. Chem. Soc.* **2010**, *132*, 2850−2851.
(27) Zhang, H.; Li, Y. J.; Ivanov, I. A.; Qu, Y. Q.; Huang, Y.; Duan, X. F. Plasmonic Modulation of the Upconversion Fluorescence in $NaYF_4$:Yb/Tm Hexaplate Nanocrystals Using Gold Nanoparticles or Nanoshells. *Angew. Chem., Int. Ed.* **2010**, *49*, 2865−2868.
(28) Schietinger, S.; Aichele, T.; Wang, H. Q.; Nann, T.; Benson, O. Plasmon-Enhanced Upconversion in Single $NaYF_4$:Yb^{3+}/Er^{3+} Co-doped Nanocrystals. *Nano Lett.* **2010**, *10*, 134−138.
(29) Zhuo, S.; Shao, M.; Xu, H.; Chen, T.; Ma, D. D. D.; Lee, S. T. Au-Modified Silicon Nanowires for Surface-Enhanced Fluorescence of Ln^{3+} (Ln = Pr, Nd, Ho, and Er). *J. Mater. Sci.: Mater. Electron.* **2013**, *24*, 324−330.
(30) Li, Z.; Wang, L.; Wang, Z.; Liu, X.; Xiong, Y. Modification of NaYF4:Yb,Er@SiO_2 Nanoparticles with Gold Nanocrystals for Tunable Green-to-Red Upconversion Emissions. *J. Phys. Chem. C* **2011**, *115*, 3291−3296.
(31) Yin, D. G.; Liu, B. H.; Zhang, L.; Wu, M. H. Preparation of a Novel Core-Shell Ag-Graphene@SiO_2 Nanocomposite for Fluorescence Enhancement. *J. Biomed. Nanotechnol.* **2012**, *8*, 458−464.
(32) Shen, J.; Li, Z. Q.; Chen, Y. R.; Chen, X. H.; Chen, Y. W.; Sun, Z.; Huang, S. M. Influence of SiO_2 Layer Thickness on Plasmon Enhanced Upconversion in Hybrid Ag/SiO_2/$NaYF_4$:Yb, Er, Gd Structures. *Appl. Surf. Sci.* **2013**, *270*, 712−717.
(33) Yuan, P.; Lee, Y. H.; Gnanasammandhan, M. K.; Guan, Z.; Zhang, Y.; Xu, Q. H. Plasmon Enhanced Upconversion Luminescence of $NaYF_4$:Yb,Er@SiO_2@Ag Core-Shell Nanocomposites for Cell Imaging. *Nanoscale* **2012**, *4*, 5132−5137.
(34) Wustholz, K. L.; Henry, A. I.; McMahon, J. M.; Freeman, R. G.; aValley, N.; Piotti, M. E.; Natan, M. J.; Schatz, G. C.; Duyne, R. P. V. Structure−Activity Relationships in Gold Nanoparticle Dimers and Trimers for Surface-Enhanced Raman Spectroscopy. *J. Am. Chem. Soc.* **2010**, *132*, 10903−10910.
(35) Liu, N.; Qin, W.; Qin, G.; Jiang, T.; Zhao, D. Highly Plasmon-Enhanced Upconversion Emissions from Au@β-$NaYF_4$:Yb,Tm Hybrid Nanostructures. *Chem. Commun.* **2011**, *47*, 7671−7673.
(36) Boyer, J. C.; Frank, C.; Van Veggel, J. M. Absolute Quantum Yield Measurements of Colloidal $NaYF_4$: Er^{3+}, Yb^{3+} Upconverting Nanoparticles. *Nanoscale* **2010**, *2*, 1417−1419.
(37) Li, X. M.; Shen, D. K.; Yang, J. P.; Yao, C.; Zhang, F.; Zhao, D. Y. Successive Layer-by-Layer Strategy for Multi-Shell Epitaxial Growth: Shell Thickness and Doping Position Dependence in Upconverting Optical Properties. *Chem. Mater.* **2013**, *25*, 106−112.
(38) Liu, Q.; Yang, T.; Feng, W.; Li, Y. F. Blue-Emissive Upconversion Nanoparticles for Low-Power-Excited Bioimaging in Vivo. *J. Am. Chem. Soc.* **2012**, *134*, 5390−5397.
(39) Yang, J. P.; Zhang, F.; Chen, Y. R.; Zhao, D. Y. Core-Shell Ag@SiO_2@mSiO_2 Mesoporous Nanocarriers for Metal-Enhanced Fluorescence. *Chem. Commun.* **2011**, *47*, 11618−11620.
(40) Yang, J.; Zhang, C.; Peng, C.; Li, C.; Wang, L.; Chai, R.; Lin, J. Controllable Red, Green, Blue (RGB) and Bright White Upconversion Luminescence of Lu_2O_3:Yb^{3+}/Er^{3+}/Tm^{3+} Nanocrystals through Single Laser Excitation at 980 nm. *Chem.—Eur. J.* **2009**, *15*, 4649−4655.
(41) Liu, S.; Zhang, Z.; Han, M. Gram-Scale Synthesis and Biofunctionalization of Silica-Coated Silver Nanoparticles for Fast Colorimetric DNA Detection. *Anal. Chem.* **2005**, *77*, 2595−2600.
(42) Vetrone, F.; Boyer, J. C.; Capobianco, J. A.; Speghini, A.; Bettinelli, M. Significance of Yb Concentration on the Upconversion Mechanisms in Codoped Y_2O_3:Er, Yb Nanocrystals. *J. Appl. Phys.* **2004**, *96*, 661.
(43) Yang, J.; Li, C.; Quan, Z.; Zhang, C.; Yang, P.; Li, Y.; Yu, C.; Lin, J. Self-Assembled 3D Flowerlike Lu_2O_3 and Lu_2O_3: Ln(3+) (Ln = Eu, Tb, Dy, Pr, Sm, Er, Ho, Tm) Microarchitectures: Ethylene Glycol-Mediated Hydrothermal Synthesis and Luminescent Properties. *J. Phys. Chem. C* **2008**, *112*, 12777−12785.
(44) Guo, H.; Yin, M.; Dong, N.; Xu, M.; Lou, L.; Zhang, W. Effect of Heat-Treatment Temperature on the Luminescent Properties of Lu_2O_3:Eu Film Prepared by Pechini Sol-Gel Method. *Appl. Surf. Sci.* **2005**, *243*, 245−250.
(45) Chen, G.; Liu, Y.; Zhang, Z.; Aghahadi, B.; Somesfalean, G.; Sun, Q.; Wang, F. Four-Photon Upconversion Induced by Infrared Diode Laser Excitation in Rare-Earth-Ion-Doped Y_2O_3 Nanocrystals. *Chem. Phys. Lett.* **2007**, *448*, 127−131.
(46) Eustis, S.; El-Sayed, M. A. Why Gold Nanoparticles Are More Precious than Pretty Gold: Noble Metal Surface Plasmon Resonance and Its Enhancement of the Radiative and Nonradiative Properties of Nanocrystals of Different Shapes. *Chem. Soc. Rev.* **2006**, *35*, 209−217.
(47) Barnes, W. L.; Dereux, A.; Ebbesen, T. W. Surface Plasmon Subwavelength Optics. *Nature* **2003**, *424*, 824−830.
(48) Le, F.; Brandl, D. W.; Urzhumov, Y. A.; Wang, H. J.; Kundu, N. J.; Aizpurua, J.; Nordlander, P. Metallic Nanoparticle Arrays: A Common Substrate for Both Surface-Enhanced Raman Scattering and Surface-Enhanced Infrared Absorption. *ACS Nano* **2008**, *2*, 707−718.
(49) Camplon, A.; Gallo, A. R.; Harris, C. B.; Robota, H. J.; Whitmore, P. M. Electronic Energy Transfer to Metal Surfaces: A Test of Classical Image Dipole Theory at Short Distances. *Chem. Phys. Lett.* **1980**, *73*, 447−450.
(50) Kummerlen, J.; Leitner, A.; Brunner, H.; Aussenegg, F. R.; Wokaun, A. Enhanced Dye Fluorescence over Silver Island Films: Analysis of the Distance Dependence. *Mol. Phys.* **1993**, *80*, 1031−1046.
(51) Lakowicz, J. R. Radiative Decay Engineering: Biophysical and Biomedical Applications. *Anal. Biochem.* **2001**, *298*, 1−24.
(52) Geddes, C. D.; Lakowicz, J. R. Metal-Enhanced Fluorescence. *J. Fluoresc.* **2002**, *12*, 121−129.
(53) Lakowicz, J. R. Plasmonics in Biology and Plasmon-Controlled Fluorescence. *Plasmonics* **2006**, *1*, 5−33.

(54) Gryczynski, I.; Malicka, J.; Shen, Y. B.; Gryczynski, Z.; Lakowicz, J. R. Multiphoton Excitation of Fluorescence Near Metallic Particles: Enhanced and Localized Excitation. *J. Phys. Chem. B* **2002**, *106*, 2191−2195.
(55) Decher, G.; Schneider, G. Distance-Dependent Fluorescence Quenching on Gold Nanoparticles Ensheathed with Layer-by-Layer Assembled Polyelectrolytes. *Nano Lett.* **2006**, *6*, 530−536.